


RESEARCH ARTICLE

Neurodegeneration and astrogliosis in the entorhinal cortex in Alzheimer's disease: Stereological layer-specific assessment and proteomic analysis

Veronica Astillero-Lopez | Melania Gonzalez-Rodriguez | Sandra Villar-Conde |
Alicia Flores-Cuadrado | Alino Martinez-Marcos | Isabel Ubeda-Banon  |
Daniel Saiz-Sanchez

Neuroplasticity and Neurodegeneration
Laboratory, CRIB, Ciudad Real Medical School,
University of Castilla-La Mancha, Ciudad Real,
Spain

Correspondence

Isabel Ubeda-Bañon, Ciudad Real Medical
School, University of Castilla-La Mancha, Avda.
Moledores S/N, 13005 Ciudad Real, Spain.
E-mail: Isabel.Ubeda@uclm.es

Funding information

UCLM/ERDF, Grant/Award Number:
2021-GRIN-31233; Spanish Ministry of
Economy and Competitiveness/ERDF,
Grant/Award Number: SAF2016-75768-R;
Spanish Ministry of Science and Innovation,
Grant/Award Number: PID2019-108659RB-
I00; Autonomous Government of Castilla-
La Mancha/ERDF, Grant/Award Number:
SBPLY/17/180501/000430

Abstract

Introduction: The entorhinal cortex is among the earliest areas involved in Alzheimer's disease. Volume reduction and neural loss in this area have been widely reported. Human entorhinal cortex atrophy is, in part, due to neural loss, but microglial and/or astroglial involvement in the different layers remains unclear. Additionally, -omic approaches in the human entorhinal cortex are scarce.

Methods: Herein, stereological layer-specific and proteomic analyses were carried out in the human brain.

Results: Neurodegeneration, microglial reduction, and astrogliosis have been demonstrated, and proteomic data have revealed relationships with up- (S100A6, PPP1R1B, BAG3, and PRDX6) and downregulated (GSK3B, SYN1, DLG4, and RAB3A) proteins. Namely, clusters of these proteins were related to synaptic, neuroinflammatory, and oxidative stress processes.

Discussion: Differential layer involvement among neural and glial populations determined by proteinopathies and identified proteins related to neurodegeneration and astrogliosis could explain how the cortical circuitry facilitates pathological spreading within the medial temporal lobe.

KEYWORDS

Alzheimer's disease, entorhinal cortex, glia, neurons, proteomic, stereology

1 | INTRODUCTION

Alzheimer's disease (AD), the most prevalent neurodegenerative disorder worldwide, is clinically defined by cognitive deficits and memory impairment.¹ Neuropathologically, it is characterized by aggregation of amyloid beta (A β) and tau proteins, which form extracellular plaques and intracellular neurofibrillary tangles, respectively.² In addition to the classic A β pathway hypothesis,³ more recently, it has been proposed that these and other pathological proteins act in a prion-like

mechanism that includes seeding (induction of naïve protein misfolding by pathological ones) and spreading (cell-to-cell transportation of misfolded proteins through neurons and/or glial cells).^{4,5} Because accumulation occurs in a predictable manner, tau allows the establishment of a six-stage neuropathological diagnosis:⁶ aggregates in early stages (Braak stage I) are found in the locus coeruleus and the entorhinal cortex (EC), from which they propagate to the hippocampal formation, the temporal cortex, and the rest of the isocortex, provoking atrophy and neurodegeneration.^{2,6-8}

This is an open access article under the terms of the [Creative Commons Attribution-NonCommercial](https://creativecommons.org/licenses/by-nc/4.0/) License, which permits use, distribution and reproduction in any medium, provided the original work is properly cited and is not used for commercial purposes.

© 2022 The Authors. *Alzheimer's & Dementia* published by Wiley Periodicals LLC on behalf of Alzheimer's Association

The EC is a transitional mesocortical structure located between the allocortical three-layered hippocampus and the typically six-layered isocortex,⁹ and it is divided into eight different subfields.¹⁰ The EC constitutes the main entrance of cortical and subcortical information into the hippocampus through the perforant pathway.¹¹ In this manner, the EC is uniquely positioned as a gateway between the cortex and the hippocampus (Figure S1 in supporting information), making it a hub from a connectomic perspective¹² essential for encoding and memory consolidation.¹³ In fact, medial temporal lobe atrophy is one of the pathological hallmarks of AD, particularly in the hippocampus and EC.¹⁴

Since the 1990s, stereological approaches using *post mortem* Nissl-stained tissue have focused on the aging hippocampus,¹⁵ reporting 68% cell loss in the cornu ammonis 1 (CA1) in AD.¹⁶ Neurodegeneration was also reported in the EC.¹⁷ Specifically, up to 90% and 70% cell loss was reported in layers II and IV, which are efferent and afferent layers, respectively.¹⁸ The percentages of NeuN-immunostained neurons in layer II varied in subsequent studies from 50%¹⁹ to 46%.²⁰ Additionally, using NeuN-immunostained material, volume fraction reduction was also reported in layer III.²¹ Thus, most previous reports have used Nissl or NeuN staining,^{20,21} which limits the discrimination of neurons from glial cells. In fact, estimates of glial cells are limited to Nissl-stained material,²¹ but specific glial markers have not been used.

Hodologically, the main efferent projections from layer II are directed through the perforant pathway to the dentate gyrus (DG), from layer III to the subiculum and CA1, which reciprocally send projections to EC layers V and VI.²² Interestingly, the loop from EC layers II and III to the DG and CA1 and back to EC layers V and VI is particularly involved in neurodegeneration.²³ Disruption of structural connectivity between the EC and hippocampus has been widely described.²⁴ However, the involvement of different pathways remains uncertain, and layer-specific EC atrophy from a connectomic/prion-like perspective is lacking. Furthermore, EC changes in AD have hardly been investigated regarding microglial²⁵ or astroglial²⁶ involvement. Finally, proteomic analyses of the human EC have only occasionally been addressed,^{27,28} elucidating dysregulation of ion transport²⁹ and phosphoprotein function³⁰ in patients with AD.

In summary, volume reduction and neuronal loss in EC have been widely reported. However, whether EC atrophy in AD patients is also due to variations in microglial and/or astroglial populations is unknown. Therefore, the aim of this work was to stereologically quantify the volume and analyze neuronal and glial changes among distinct layers of the human EC. Simultaneously, a proteomic analysis was performed to identify possible markers of these changes in AD that have revealed different protein clusters involving synaptic, neuroinflammatory, and oxidative stress processes.

2 | METHODS

2.1 | Human samples

Post mortem human brain samples of EC were provided by IDIBAPS, BIOBANC-MUR, BTCIEN, and BPA, integrated in the Spanish National Biobanks Network, and then processed following standard operating

RESEARCH IN CONTEXT

1. Systematic review: The entorhinal cortex (EC) is among the earliest areas involved in Alzheimer's disease (AD). Human EC atrophy is, in part, due to neural loss, but microglial, and/or astroglial involvement in the different layers remains unclear. Additionally, -omic approaches in this area are scarce. Herein, stereological layer-specific and proteomic analyses have been carried out in the human brain.
2. Interpretation: Neurodegeneration, microglia reduction, and astrogliosis have been demonstrated and proteomic data have revealed relationships with up- (S100A6, PPP1R1B, BAG3, and PRDX6) and downregulated (GSK3B, SYN1, DLG4, and RAB3A) proteins. Namely, clusters of these proteins were related with synaptic, neuroinflammatory, and oxidative stress processes.
3. Future directions: Several novel proteins reported here could play a fundamental role in the pathogenesis of AD and seem to have a functional link with neurons and glial cells. These results provide new insights into the coordinated control of AD proteins and their cell-type-specific contribution to disease susceptibility.

procedures with the approval of the Ethical and Scientific Committees and the Ethical Committee of Clinical Research at Ciudad Real University Hospital (SAF2016-75768-R and PID2019-108659RB-I00).

Two experimental groups were used: N = 20 AD cases (only patients neuropathologically diagnosed with Braak stages V and VI AD were selected to ensure sample homogeneity) and N = 18 age-matched non-AD cases (Table 1). Nine cases of each experimental group (mean age \pm standard error of the mean [SEM]: 80.78 \pm 1.928, n = 9 AD; 72.22 \pm 4.371, n = 9 non-AD; P value = .092), which were received as formalin-fixed embedded blocks, were used for histological procedures and stereology. Fresh-frozen tissue blocks were used to perform the proteomic analysis and technical validation using western blotting (mean age \pm SEM: 78.50 \pm 1.688, n = 6 AD; 62.75 \pm 10.00, n = 4 non-AD; P value = .281). Ten additional cases (mean age \pm SEM: 78.60 \pm 5.085, n = 5 AD; and 75.60 \pm 3.265, n = 5 non-AD; P value = .793) were used for biological validation using western blotting (Figure S2 in supporting information).

2.2 | Histological procedures

Human tissue was processed for histological procedures as previously reported,³¹ and sections were selected from levels 16.0 to 23.9 mm from bregma.³² Protocols for immunohistochemistry and immunofluorescence are detailed in the supporting information.

TABLE 1 Demographic and clinic-pathological features of the individuals used in the present study

Case	DxAP	Braak Stage	Assay	TDP43	Sex	Age (years)	PMD (hh:mm)	Brain weight (g)	Disease duration (years)	Original fixation	Cause of death	BSL (mm)
1	AD	V	IH, IF	Negative	F	74	4:00	1042	5	Formaldehyde	Cardiorespiratory arrest	16.0-17.2
2	AD	V	IH, IF	Unrealized	F	80	4:00	910	n.a.	Formaldehyde	Respiratory infection	16.0-17.2
3	AD	VI	IH, IF	Unrealized	M	77	5:00	1330	n.a.	Formaldehyde	Sepsis of bacterial origin	18.6-19.9
4	AD	V	IH, IF	Negative	F	84	2:00	920	11	Formaldehyde	n.a.	18.6-19.9
5	AD	VI	IH, IF	Negative HIP	M	77	6:00	1060	10	Formaldehyde	Acute respiratory infection	18.6-19.9
6	AD	V	IH	Negative HIP/A	M	75	3:00	1050	4	Formaldehyde	Multi-organic failure	21.2-22.6
7	AD	VI	IH, IF	Negative HIP/A	F	83	2:00	1000	9	Formaldehyde	Respiratory failure	21.2-22.6
8	AD	VI	IH, IF	Negative HIP/A	F	85	2:00	1150	7	Formaldehyde	Cardiorespiratory arrest	22.6-23.9
9	AD	VI	IH	Positive HIP/A; Negative FC (LATE 2)	M	92	6:00	960	n.a.	Formaldehyde	n.a.	22.6-23.9
10	AD	VI	PR, WB	Negative HIP	F	81	0:27	935	15	Frozen no-fix	n.a.	-
11	AD	VI	PR, WB	Negative HIP	F	75	16:15	n.a.	n.a.	Frozen no-fix	n.a.	-
12	AD	VI	PR, WB	Negative HIP	M	80	21:45	n.a.	n.a.	Frozen no-fix	n.a.	-
13	AD	VI	PR, WB	Negative HIP	F	80	5:00	1060	8.5	Frozen no-fix	Acute heart failure	-
14	AD	VI	PR, WB	Negative HIP	F	72	14:00	n.a.	n.a.	Frozen no-fix	n.a.	-
15	AD	V	PR, WB	Negative HIP	M	83	5:00	n.a.	n.a.	Frozen no-fix	n.a.	-
16	AD	VI	WB	Positive HIP	M	90	4:30	1070	9	Frozen no-fix	Cardiorespiratory arrest	-
17	AD	V	WB	Positive	F	91	5:00	n.a.	n.a.	Frozen no-fix	n.a.	-
18	AD	VI	WB	Negative	F	76	11:10	900	n.a.	Frozen no-fix	Cardiorespiratory arrest	-
19	AD	VI	WB	Negative	M	69	2:25	n.a.	n.a.	Frozen no-fix	Multi-organic failure	-
20	AD	VI	WB	Negative	F	67	4:15	n.a.	n.a.	Frozen no-fix	Neumonía broncoaspirativa	-
21	NAD	-	IH, IF	Negative HIP/A	F	81	5:00	1100	-	Formaldehyde	Multi-organic failure	16.0-17.2
22	NAD	-	IH, IF	Negative HIP/A	M	84	3:00	1400	-	Formaldehyde	Cardiorespiratory arrest	17.2-18.6
23	NAD	-	IH	Negative HIP/A	M	78	4:00	1100	-	Formaldehyde	Respiratory failure	19.9-21.2

(Continues)

TABLE 1 (Continued)

Case	DxAP	Assay	Braak Stage	TDP43	Sex	Age (years)	PMD (hh:mm)	Brain weight (g)	Disease duration (years)	Original fixation	Cause of death	BSL (mm)
24	NAD	IH	-	Negative HIP/A	M	53	5:00	1300	-	Formaldehyde	Cardiorespiratory arrest	19.9-21.2
25	NAD	IH	II	Negative HIP	M	88	3:00	1285	-	Formaldehyde	n.a.	19.9-21.2
26	NAD	IH	-	Negative HIP/A	M	58	6:00	1500	-	Formaldehyde	Acute myocardial infarction	21.2-22.6
27	NAD	IH	-	Negative HIP/A	M	63	2:00	1400	-	Formaldehyde	Cardiorespiratory arrest	21.2-22.6
28	NAD	IH, IF	-	Negative HIP/A	F	62	2:00	1050	-	Formaldehyde	Cardiorespiratory arrest	22.6-23.9
29	NAD	IH	II	Negative HIP	M	83	n.a.	1152	-	Formaldehyde	n.a.	22.6-23.9
30	NAD	PR, WB	-	Negative HIP	M	73	6:10	1030	-	Frozen no-fix	Respiratory infection	-
31	NAD	PR, WB	-	Negative HIP	M	83	13	1630	-	Frozen no-fix	n.a.	-
32	NAD	PR, WB	-	Negative HIP/A	F	37	9:00	1200	-	Frozen no-fix	Septic shock	-
33	NAD	PR, WB	-	Negative HIP/A	M	58	5:00	1300	-	Frozen no-fix	Cerebral haemorrhage	-
34	NAD	WB	-	Negative HIP	F	83	7:20	1320	-	Frozen no-fix	Intestinal ischemia	-
35	NAD	WB	-	Negative	M	77	10:31	n.a.	-	Frozen no-fix	n.a.	-
36	NAD	WB	-	Negative	M	68	4:10	1350	-	Frozen no-fix	Sepsis	-
37	NAD	WB	-	Negative	F	82	4:00	800	-	Frozen no-fix	Respiratory failure	-
38	NAD	WB	-	Negative	M	68	4:00	1220	-	Frozen no-fix	Cardiorespiratory arrest	-

Abbreviations: A, amygdala; AD, Alzheimer's disease; BSL, Bregma study levels; DxAP: neuropathological diagnosis; F, female; FC, frontal cortex; HIP, hippocampus; IF, immunohistochemistry; IH, immunofluorescence; M, male; n.a., not available; NAD, non-Alzheimer's disease; PMD, *post mortem* delay; PR, proteomic; WB, western blot.

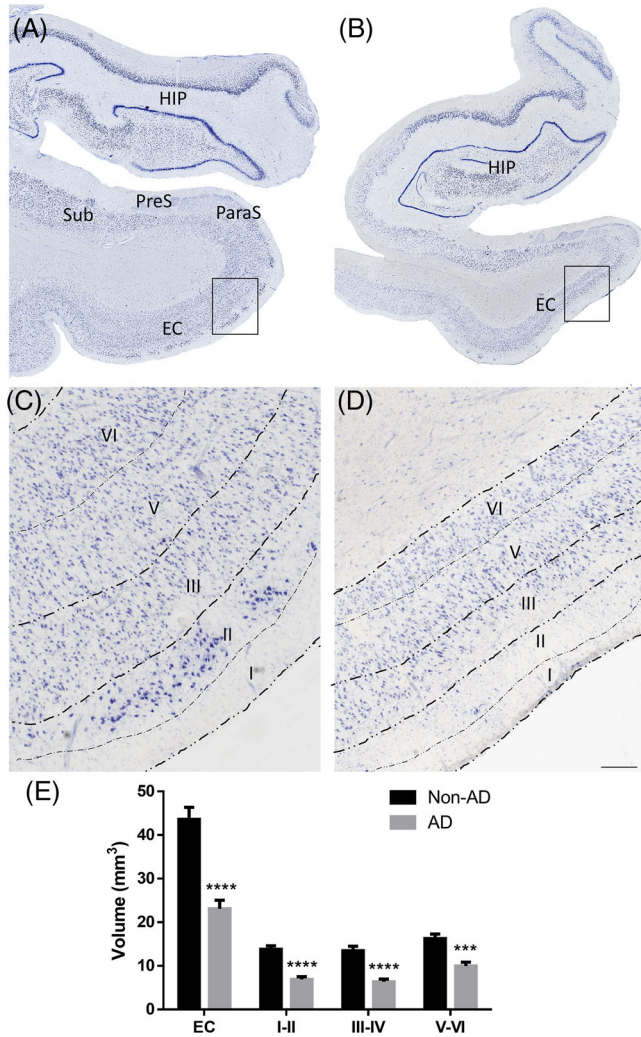


FIGURE 1 Cytoarchitecture and volume quantification of the human EC. Mosaic reconstruction of coronal Nissl-stained sections of the human EC (bregma 16.0 to 17.2 mm) and details of its layers in non-AD (A and C, respectively) and AD (B and D, respectively) cases. Darker lines indicate separation of layers analyzed in the present study between groups. Note the absence of layer IV in this bregma level. The graph shows the mean total volume \pm standard error of the mean of the EC (E). Scale bars for A, B = 1000 μ m and C, D = 155 μ m. AD, Alzheimer's disease; EC, entorhinal cortex; HIP, hippocampus; PreS, presubiculum; ParaS, parasubiculum; Sub, subiculum

2.3 | Stereological quantification

For stereological quantification, layers I and II, layers III and IV, and layers V and VI were outlined based on Nissl staining and well-known cytoarchitectonic characteristics (Figure 1A-D).⁹

Stereological quantifications of volume and neuronal and glial populations were obtained using Stereo Investigator 9.0 software (MBF Bioscience) coupled to a Zeiss Axio Imager M2 microscope (Carl Zeiss). Volumetric quantification was performed using the Cavalieri method (Plan-Neofluar 1x/0.025, Ref. 420300-9900). The total number of neu-

rons, microglia, or astroglia was determined in NeuN-, Iba-1-, or glial fibrillary acidic protein (GFAP)-immunostained preparations using the Optical Fractionator probe (Plan Apochromat, 63x/1.4, oil lens, Ref. 420782-9900). The area fractions occupied by A β , GFAP, and tau were analyzed by Area Fraction Fractionator probe (Plan Apochromat 20x/0.5, Ref. 420650-9901). Four tissue sections per case were used. The Gundersen error coefficient was < 0.1 (for details see Tables S2, S3, S4, S5, and S6 in supporting information).

2.4 | Proteomic analysis

Proteins were extracted from frozen samples with radioimmunoprecipitation assay (RIPA) buffer, and global protein profiles obtained by sequential window acquisition of all theoretical fragment ion spectra mass spectrometry (SWATH-MS) were analyzed using data-dependent acquisition (DDA) shotgun nanoscale liquid chromatography coupled to tandem mass spectrometry (nanoLC-MS/MS) runs described in previous protocols³¹ (see the supporting information). Proteomic analysis was carried out at the Instituto Maimónides de Investigación Biomédica de Córdoba Proteomic Facility. Prior to the bioinformatics analysis, Excel was used to normalize protein abundance by log transformation and to filter for fold change and/or p value. Principal components analysis (PCA), heatmap, and volcano plots were constructed using proteins with a P-value $< .05$ in MetaboAnalyst version 5.0 software (<https://www.metaboanalyst.ca/>). Differentially expressed proteins were established with a P value $< .01$ and thresholds set to ≥ 2 for upregulation and ≤ 0.5 for downregulation. These proteins were classified in The Gene Ontology Resource (<http://geneontology.org/>) by Gene Ontology terms based on a given protein's biological processes, molecular functions, or cellular components. Proteomic pathways were analyzed using Reactome databases (<https://reactome.org/>). Finally, the STRING website (<https://string-db.org/>) was used to establish the protein-protein interaction networks of some differentially expressed proteins and to create four cluster networks with the kmeans algorithm. The mass spectrometry proteomics data have been deposited to the ProteomeXchange Consortium (<http://proteomecentral.proteomexchange.org>) via the PRIDE partner repository with the dataset identifier PXD029359 (Username: reviewer_pxd029359@ebi.ac.uk; Password: 9ZBBqh6c).

2.5 | Western blot

Two experimental groups were used for technical (n = 4 non-AD and n = 6 AD) and biological (n = 5 non-AD and n = 5 AD) validation using western blotting (Table 1, Figure S2).

Protein concentration was determined using a Bicinchoninic Acid Kit for Protein Determination (Sigma-Aldrich) and a Multiskan™ FC Microplate Photometer (Thermo Fisher Scientific). Equal amounts of protein lysates (30 μ g) from human samples were loaded onto 10% polyacrylamide gels for sodium dodecyl sulfate polyacrylamide

gel electrophoresis (SDS-PAGE), and electrophoretically transferred to polyvinylidene difluoride (PVDF) membranes. Membranes were blocked with nonfat dry milk or bovine serum albumin (BSA) in TTBS (1% TBS pH 8.8 plus 0.5% Tween) for 60 minutes and incubated with primary antibodies (Table S1 in supporting information) overnight at 4°C. Membranes were then washed with TTBS and incubated with appropriate peroxidase-conjugated secondary antibodies. Band intensity was imaged with Syngene G:BOX (GeneSys software) after incubation with enhanced chemiluminescence reagents (Thermo Fisher Scientific) and analyzed with ImageJ.

2.6 | Statistics

Statistical analyses of the stereological study and western blots were conducted using GraphPad Prism 6 software (GraphPad Inc., v.6). Data are presented as the mean \pm SEM, and statistical comparisons were made using either *t*-tests or Mann–Whitney U tests and using one-way analysis of variance or the Kruskal–Wallis test when several variables were compared. The Rout test was used to identify any outliers. The statistical significance level was established at $\alpha = 0.05$. Significant differences are marked as **P* value < .05, ***P* value < .01, ****P* value < .001, and *****P* value < .0001.

3 | RESULTS

3.1 | Volume

Mosaic reconstructions of the whole hippocampal gyrus in non-AD (Figure 1A) and AD (Figure 1B) cases showed atrophy, which was particularly evident in the different layers of the EC (Figure 1C, D). Quantitative volume estimates showed a substantial reduction in the whole EC and its different layers in AD cases compared to non-AD cases (Figure 1E, Table S2).

3.2 | Neuronal and glial quantification

Images of immunohistochemistry against NeuN (Figure 2A, B), Iba-1 (Figure 2E, F), and GFAP (Figure 2I, J) showed different staining patterns in non-AD and AD cases. In fact, stereological quantification revealed a significant reduction in the total number of NeuN-positive cells in the whole EC and its different layers, particularly in layers III and IV (Figure 2C), but not regarding cell density in the AD group (Figure 2D). Iba-1 quantification also revealed a significant decrease in the total number of cells in the whole EC and in layers I and II and V and VI in AD cases (Figure 2G), but no changes in density were detected (Figure 2H). Conversely, GFAP quantification did not reveal changes in the total number of cells (Figure 2K), but the density was significantly higher in the whole EC and layers I and II and III and IV in the AD group (Figure 2L; see also Tables S3, S4, and S5).

3.3 | Characterization of tau and A β pathology and astroglia

To assess the correlations among pathological markers and the higher density expression of astroglial markers (Figure 2L), we performed triple immunofluorescence of A β , tau, and GFAP proteins in the EC (Figure 3A), analyzing its different layers (Figure 3B–D). Regarding pathological markers, tau was significantly more abundant in the EC than A β expression, and tau deposits were also significantly higher in layers I and II and layers III and IV than in layers V and VI (Figure 3E). The area fraction occupied by GFAP was significantly higher in layers I and II than in layers III and VI (Figure 3F, Table S6). Overlapping percentages indicate that GFAP mostly overlaps with tau in all layers compared to A β (Figure 3G).

Proteomic analysis

In the SWATH-MS proteomic analysis, a total of 1635 proteins were identified in the human EC (Table S7 in supporting information). PCA showed separation of the AD and non-AD groups (Figure 4A), and the heatmap revealed different patterns in both groups (Figure 4B). Comparing the distribution of abundant proteins by volcano plot, 103 proteins were commonly affected, 42 were upregulated and 61 were downregulated (Figure 4C, Table S8 in supporting information). Enriched Gene Ontology terms in biological processes, molecular functions, and cellular components were obtained from differentially expressed proteins (Table S9 in supporting information). The affected pathways were analyzed by Reactome, indicating that pathways dysregulated in the human EC in AD were related to neuronal and immune systems, including substantial alterations in axon guidance, vesicle cycle processes, and synapse function (Figure 4D, Table S10 in supporting information). Most of the proteins showed close interactions with each other in the STRING analysis (Figure 4E, Table S11 in supporting information). Four different clusters related to synapses and inflammation (green), axonal formation (red), vesicular transport (blue), and chaperone response (yellow) were identified. Interestingly, neuronal (KIF5C), astroglial (GFAP), and microglial (AIF1) proteins identified in STRING correlated with cell populations analyzed in stereology (asterisks in Figure 4E). Furthermore, the upregulated proteins GFAP and vimentin indicated reactive gliosis and an inflammatory state.

3.4 | Validation of proteomic results

After SWATH-MS proteomic and bioinformatics analyses, eight proteins were selected (four upregulated proteins: S100A6, PPP1R1B, BAG3, and PRDX6, and four downregulated proteins: GSK3B, SYN1, DLG4, and RAB3A) based on different criteria. The first criterion was statistical significance and the second was based on functional interactions extracted from the STRING analysis and their associations

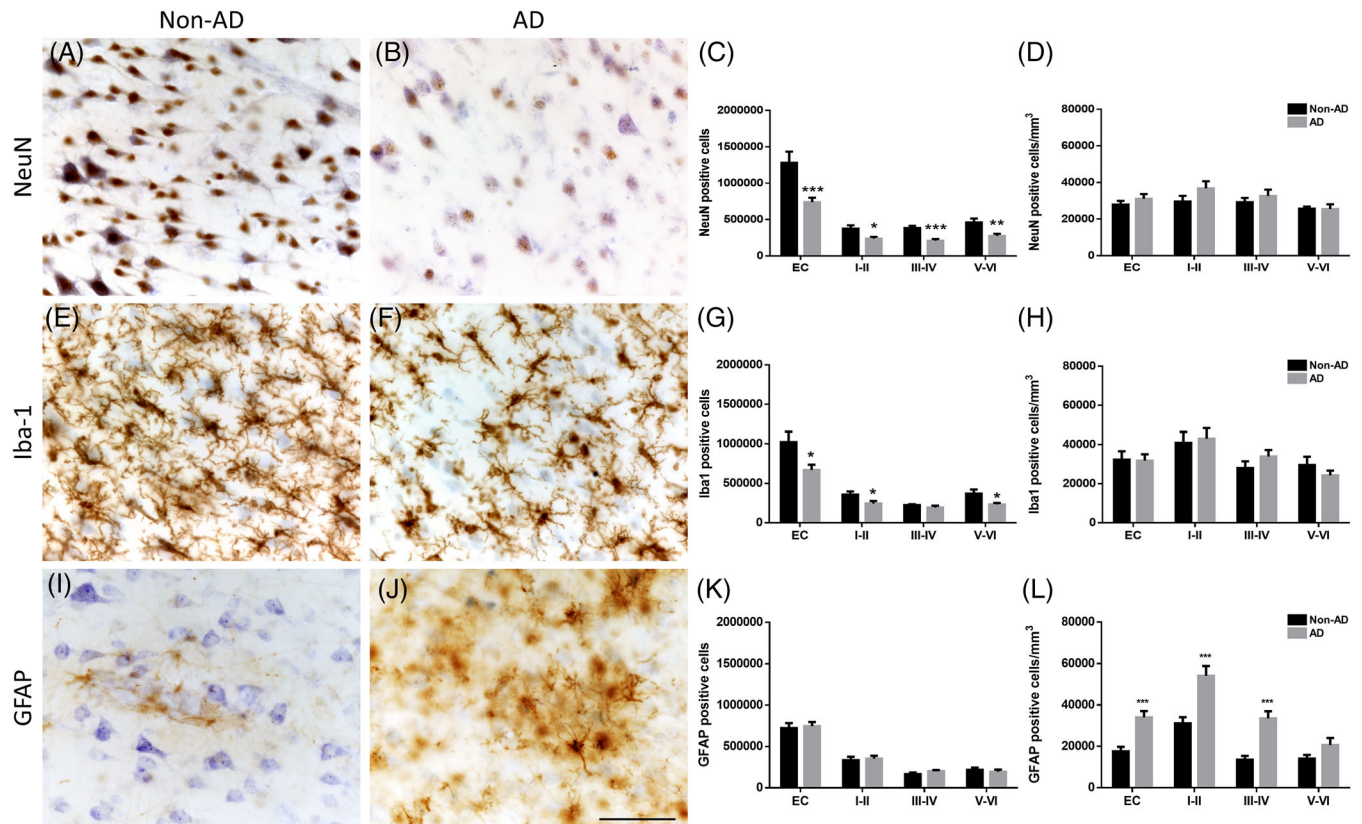


FIGURE 2 Stereological quantification of NeuN⁺, Iba-1⁺, and GFAP⁺ cells in the human EC. Coronal sections of the human EC were immunohistochemically stained for NeuN (A-B), Iba-1 (E-F), and GFAP (I-J) in the non-AD and AD groups. The mean values \pm standard error of the mean for NeuN (C-D), Iba-1 (G-H), and GFAP (K-L)-positive cells and the density of the total EC and its layers. The intensity of NeuN labeling was noticeably lower in AD cases, showing profound neurodegeneration along with an atrophic morphology of the remaining neurons (B). Differences in astrocyte staining patterns, along with more extensive processes, are observed in AD (J) compared to non-AD cases, suggesting possible astrocyte hyperresponsiveness. Scale bar = 50 μ m. AD, Alzheimer's disease; EC, entorhinal cortex

with both stereological (neurons-KIF5C, microglia-AIF1, and astroglia-GFAP) and pathological markers ($A\beta$ and tau). These proteins were validated qualitatively (immunofluorescence) and quantitatively (technical and biological validation using western blotting; Figure S2).

3.4.1 | Qualitative validation by immunofluorescence

Immunofluorescence with stereological markers of neurons (NeuN or, alternatively, PAN to achieve multilabeling), microglia (Iba-1), and astroglia (GFAP) and selected proteins was performed to validate the SWATH-MS analysis and to assess spatial relationships. In addition, the pathological relationships with $A\beta$ and tau were investigated with some selected proteins.

S100A6 (corresponding to the S100 α 6 antibody; Figure S3A, D in supporting information), PPP1R1B (corresponding to the DARPP32 antibody; Figure S4A, C in supporting information), BAG3 (Figure S5A, D in supporting information), and PRDX6 (Figure S6A, D in supporting information) levels were higher in AD. The distribution of these proteins was investigated in non-AD and AD cases by performing stain-

ing for astrocyte maker (Figures S3B, E; S4B, D; S5 B, C, E, F; S6C, F). S100A6 showed a relationship with neurons (Figure S3C, F). PRDX6 overlapped with microglial cells (Figure S6B, E).

On the other hand, GSK3B (corresponding to GSK3 β antibody; Figure S7A, C in supporting information), SYN1 (Figure S8A, C in supporting information), and DLG4 (corresponding to PSD95 antibody; Figure S9A, D in supporting information) levels were lower in AD. Although RAB3A was downregulated in the proteomic study, immunofluorescence staining revealed an apparent increase in its expression levels in AD (Figure S10A, C in supporting information). GSK3B and RAB3A showed spatial localization in neuronal cells (Figures S7 and S10). SYN1 colocalized with astrocytes in non-AD (Figure S8B), but not in AD (Figure S8D). DLG4 colocalized with microglial cells in non-AD (Figure S9C) but not in AD (Figure S9F) and was expressed in astrocytes (Figure S9B, E). Regarding $A\beta$ and tau pathology, S100A6 (Figure S3E), BAG3 (Figure S5F), and PRDX6 (Figure S6E, F) were associated with the $A\beta$ peptide in AD cases. Moreover, BAG3 was found in the vicinity of tau deposits (Figure S5E). Representative images of orthogonal views from z-stacks are shown in Figure 5 to confirm antibody colocalizations between selected proteins, stereological markers, and pathological proteins.

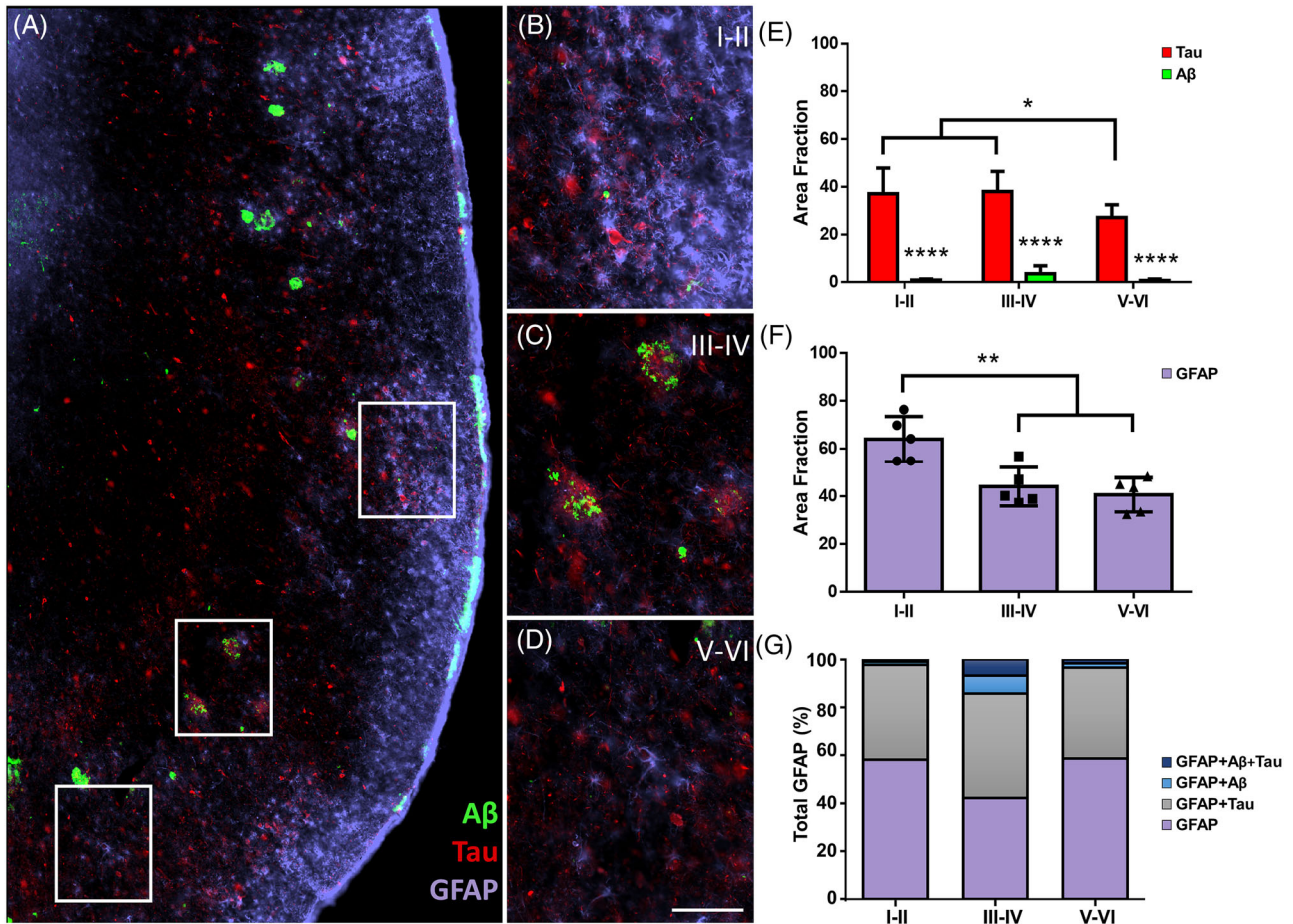


FIGURE 3 Characterization of amyloid beta ($A\beta$) and tau pathology and their spatial distributions with astrocytes. (A) Mosaic reconstruction of EC coronal sections from AD cases immunofluorescently stained for $A\beta$ (green), tau (red) and GFAP (purple). Details of layers I and II (B), III and IV (C) and V and VI (D). The mean area fractions \pm standard error of the mean occupied by tau, $A\beta$, and GFAP in the different layers of the EC (E and F, respectively). Total GFAP percentage area fraction and overlap in the different EC layers (G). Scale bars for A = 250 μ m and B, C, D = 100 μ m. $A\beta$, amyloid beta; AD, Alzheimer's disease; EC, entorhinal cortex; GFAP, glial fibrillary acidic protein

3.4.2 | Quantitative technical validation using western blotting

Western blotting of the same cases used in the SWATH-MS study was performed (Figure S2). According to SWATH-MS analyses, BAG3 and PRDX6 were expressed at significantly higher levels in AD cases. In contrast to the SWATH-MS results, western blot analysis showed higher expression of RAB3A in AD patients. No statistically significant differences were found for S100A6, PPP1R1B, GSK3B, DLG4, or SYN1 (Figures S11 and S12 in supporting information).

3.4.3 | Quantitative biological validation using western blotting

Western blotting of different cases used in the SWATH-MS analysis was carried out (Figure S2). Consistent with SWATH-MS analyses, S100A6, PRDX6, and GFAP were expressed at significantly higher levels in AD cases. No statistically significant differences were observed

in PPP1R1B, GSK3B, DLG4, or SYN1 (Figure S12 and S13 in supporting information).

4 | DISCUSSION

The present study represents a complementary stereological and proteomic approach to characterize changes in the human EC in AD. Layer-specific analyses of neural and glial involvement and correlations with pathological markers were performed and will be discussed in terms of prionoid and connectomic perspectives. In parallel, up- and downregulated identified proteins will be correlated with processes underlying neurodegeneration and astrogliosis.

Limitations of the study due to the relatively low number of cases used in the proteomic analysis have been counterbalanced using very restrictive cut-off parameters and performing double validation: immunofluorescence-confocal microscopy and western blotting (including technical and biological testing using additional cases). A complete correlation was not observed between techniques given the

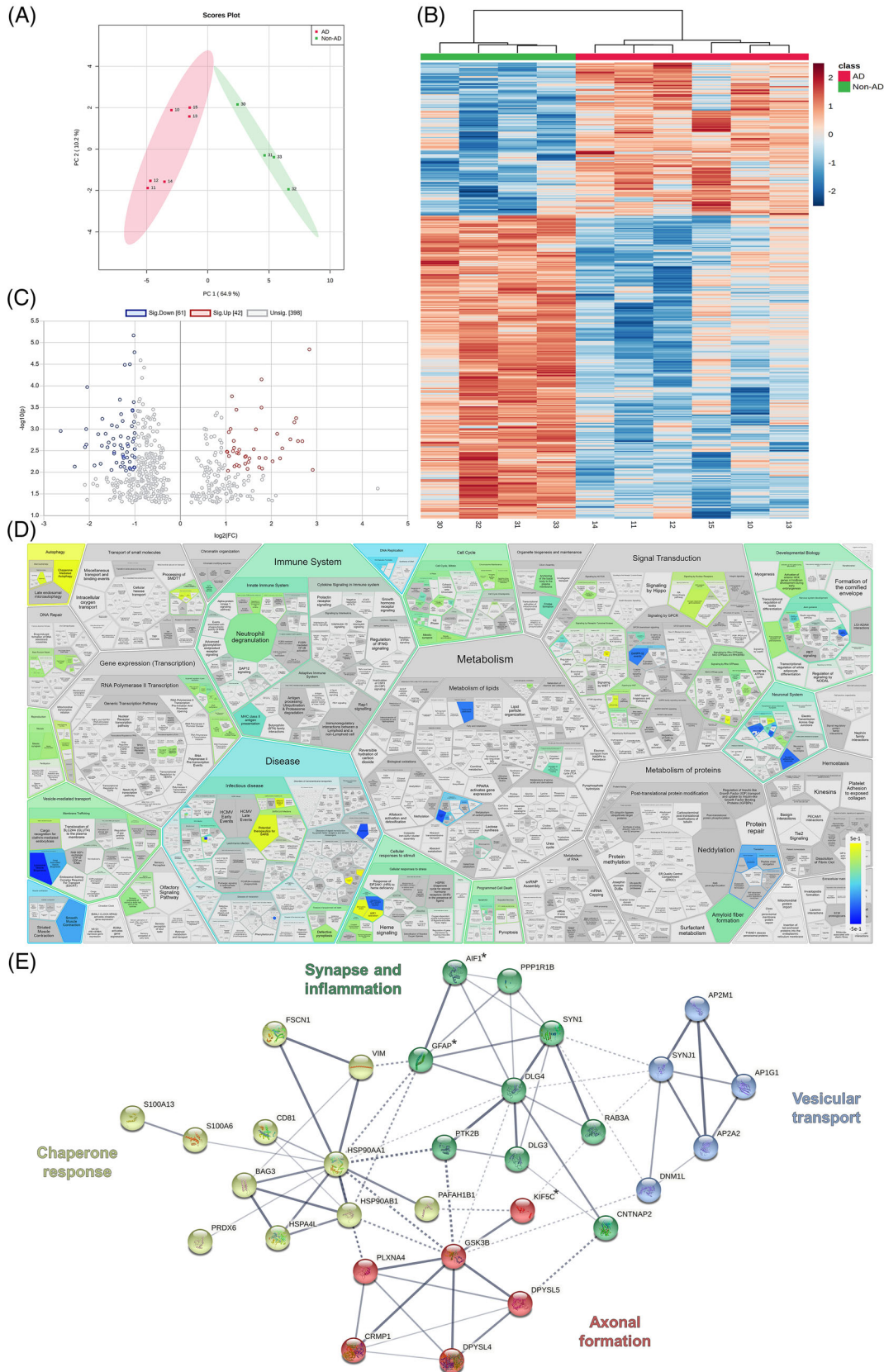


FIGURE 4 Proteomic analyses. (A) Principal component analysis showing two well-separated groups (P value $< .05$): non-Alzheimer's disease (AD; green) and AD (red). (B) Heatmap revealing the differential expression of 1635 proteins between groups (P value $< .05$). (C) Volcano plot showing 42 upregulated and 61 downregulated proteins with a fold change ≥ 2 (or ≤ 0.5) and $P < .01$. (D) Reactome pathways altered in AD cases. (E) STRING analysis of 33 differentially expressed proteins (represented with nodes) distributed in four network clusters; asterisks indicate markers used for stereology or equivalent

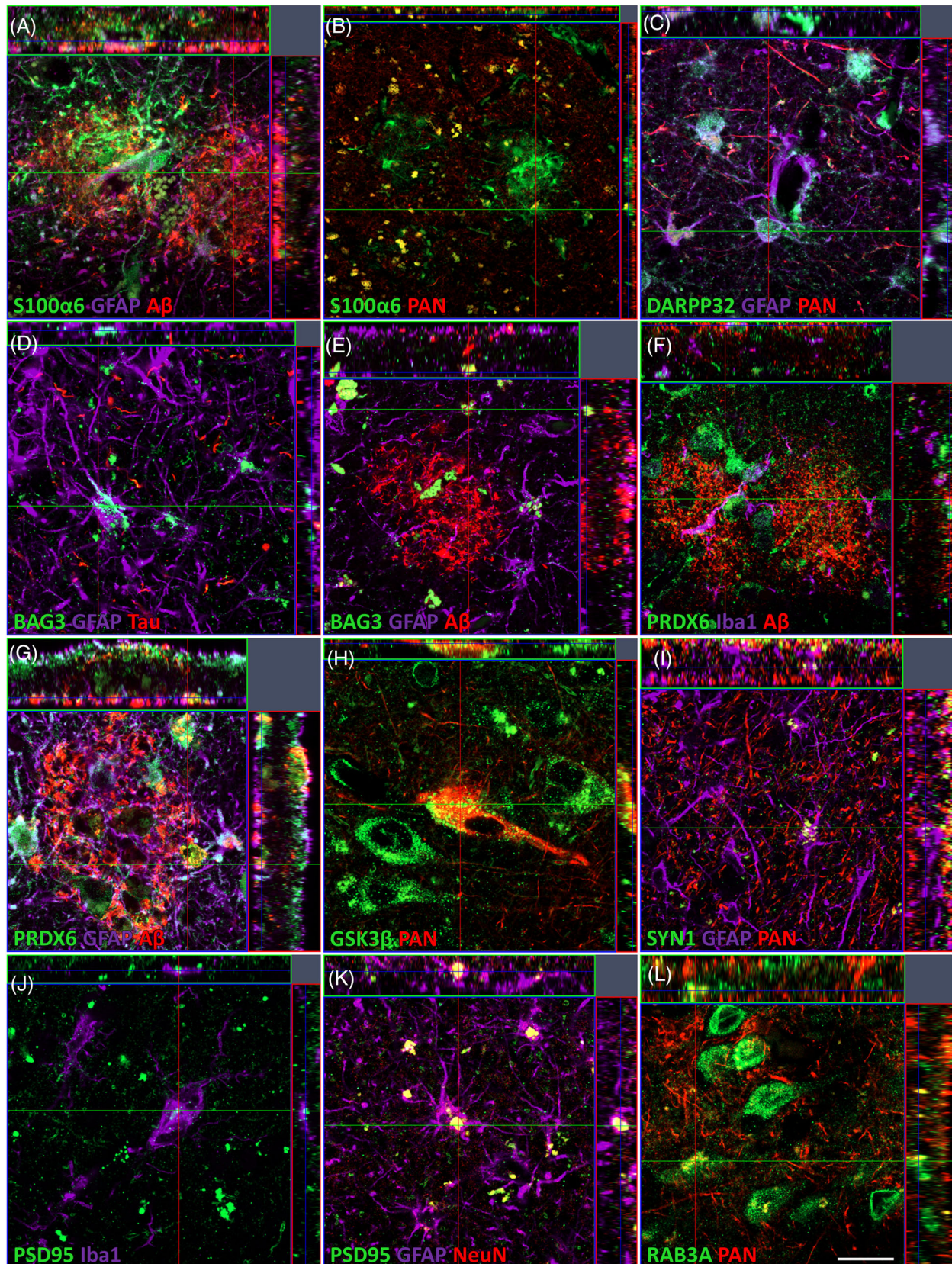


FIGURE 5 Validation of proteomic results using immunofluorescence. Orthogonal views of z-stacks showing the colocalization among selected proteins, stereological markers, and pathological proteins. Coronal sections of the human EC immunofluorescently stained for selected proteins (S100A6-S100 α 6 antibody, PPP1R1B-DARPP32 antibody, BAG3, PRDX6, GSK3B-GSK3 β antibody, SYN1, DLG4-PSD95 antibody, and RAB3A), stereological markers (NeuN, or alternatively PAN, for neurons, Iba-1 for microglia, and GFAP for astrocytes) and A β and tau pathological markers. Z-stack images were captured with a Zeiss LSM 800 confocal microscope coupled to Zen 2.3 software. Each z-stack correspond to a specific number of slices. Scale bar = 20 μ m for A and C-L; scale bar = 60 μ m for B. A β , amyloid beta; AD, Alzheimer's disease; EC, entorhinal cortex; GFAP, glial fibrillary acidic protein

substantial variability among human samples and due to the possible lack of specificity of commercially available antibodies. Regarding sex and age, the availability of samples did not allow us to balance sex, and no age differences among groups were detected. Possible comorbidities with TDP-43 have been considered and are limited to three cases (Table 1).³³

Unbiased stereological estimations of volume and neuronal, microglial, and astroglial populations of EC layers were carried out. In agreement with previous studies, we detected a severe 50% volume reduction in the whole EC. Specifically, estimates revealed 50.2%, 52.7%, and 38.64% volume reductions in layers I and II, III and IV, and V and VI, respectively (Figure 1). Consistent with previous reports,¹⁸ the most profound neurodegeneration was present in layers II through IV (supragranular layers; note that layer IV corresponds to the granular layer that is poorly represented in some areas of the EC) compared to layers V and VI (infragranular layers), which interestingly show hierarchical connectivity patterns.³⁴ Neurodegeneration, therefore, has been widely reported in the EC, but glial involvement has been poorly studied.³⁵

Regarding stereological estimates of glial populations, our data show microglial loss in the EC of AD patients, which was previously unreported. Although layers III and IV were unaffected, layers I and II and V and VI revealed cell losses of 31.9% and 37%, respectively (Figure 2). No changes in the number of astrocytes were observed between AD and non-AD patients, but the density of GFAP cells was significantly higher in layers I and II and III and IV and the EC in AD with percentages of 42.5%, 59.7%, and 48.3%, respectively, which might indicate a lower vulnerability of astrocytes to AD than neuronal and microglial populations. However, morphological changes observed in astrocytes (Figure 2) suggest astrogliosis.²⁵ Interestingly, the GFAP area fraction revealed particularly notable astrogliosis in layers I and II (Figure 3F).

Concerning pathology, the EC is involved early in stage I by tauopathy.⁶ Our analysis showed profound tau deposition compared to A β pathology, particularly in layers I through IV (Figure 3E). Although not significant, A β levels were higher in layer III, which in turn projects to CA1, the most affected region in the hippocampus.¹⁶ From a prionoid and connectomic perspective,^{12,23} the EC has been described as a hub because it is essential for memory encoding and retrieval.³⁶ In this sense, superficial layers II and III send efferents to GD, CA2-CA3, and CA1 and the subiculum, respectively. Deeper layer V receives hippocampal afferents from CA1 and the subiculum and projects to the isocortex.^{22,37} Therefore, the neurodegeneration and tauopathy in specific layers reported here may be explained by this entorhino-hippocampal far-forward loop involving earliest and more severely supragranular rather than infragranular layers.^{34,38}

According to our proteomic analysis, four upregulated proteins (S100A6, PPR1B1B, BAG3, and PRDX6) and four downregulated proteins (GSK3B, SYN1, DLG4, and RAB3A) and their possible relationships with neurons, microglia, and/or astroglia or pathology were further investigated (Figures 4 and 5).

S100A6 was the second highest protein in the present study. It has been found in subpopulations of neurons and astrocytes in the brain.³⁹ We report that S100A6, although it colocalized with neurons in the

EC, is particularly expressed in astroglial cells. Intriguingly, this protein accumulated in astrocytes surrounding the A β plaques, consistent with astrocyte activation (Figures 5A, B and S3). A function of this protein in degrading A β aggregates has been proposed.⁴⁰ Moreover, this protein might have a neuroprotective role in early stages or exacerbate disease pathology in later stages.⁴¹

PPP1R1B, a key inhibitor of protein phosphatase-1 (PP-1), plays a fundamental role in dopaminergic neurotransmission and is crucial for synaptic function.⁴² We report for the first time a higher expression of PPP1R1B in AD and its relationship with astrocytes (Figures 5C and S4).

Confocal studies revealed that BAG3 was also upregulated in astrocytes of AD patients. BAG3 participates in the maintenance of healthy synapses through tau autophagic postsynaptic clearance.⁴³ Herein, we demonstrated the presence of this protein around tau aggregates and its association with A β pathology (Figures 5D, E, and S5), which supports previous observations of astroglial clearance function.³⁵

PRDX6 is an antioxidant enzyme primarily found in human brain astrocytes.⁴⁴ PRDX6 was upregulated in our study, coexpressing both astroglial and microglial markers, and was related to A β aggregates (Figures 5F, G, and S6). Consistent with other studies,⁴⁵ microglia were found in the vicinity of plaques, whereas astrocytes were placed within and surrounding A β aggregates. Therefore, PRDX6 may be related to a protective mechanism against oxidative stress in the human EC.⁴⁶

GSK3B, the main kinase phosphorylating tau protein,⁴⁷ showed reduced expression in EC in AD and overlapped with neurons (Figures 5H and S7). GSK3B is associated with cognitive function and has been used as a cerebrospinal fluid biomarker, because GSK3B inhibitors reduce AD pathology.^{48,49}

SYN1, DLG4, and RAB3A, which have been described to be essential for synaptic function,^{50–52} were expressed at lower levels in AD. Our data agree with other studies showing altered synapse function.⁵³ Decreases in SYN1 in the CA1 region and DG of the hippocampus in AD patients have been previously reported,⁵⁴ but studies in human EC are lacking. We report here a reduction in SYN1 levels in the human EC in AD and spatial colocalization with astrocytes (Figure 5I and S8). Low presynaptic SYN1 levels may also exert a negative effect on the postsynaptic level, where DLG4 was downregulated.^{50,51} The literature is controversial regarding how DLG4 protein levels are affected in the AD brain.⁵⁵ Our proteomic study revealed a marked reduction in this protein. We also wanted to confirm that DLG4, which is found in neurons, correlated with microglia (AIF1) and astroglia (GFAP) in the EC, as shown by STRING analysis (Figure 4E). In fact, DLG4 overlapped with both glial cell populations, especially in astroglia (Figure 5J, K, and S9). On the other hand, the presence of SYN1 and DLG4 proteins in astrocytes may be related to tripartite synapses.⁵⁶ RAB3A is a presynaptic protein involved in vesicle recycling to maintain healthy synaptic units.⁵⁷ SWATH-MS analyses revealed RAB3A to be a downregulated protein in AD. However, its expression was significantly higher in WB and confocal analyses, where RAB3A showed a typical neuronal morphology (Figure S5L and S10). Interestingly, higher RAB3A expression in astrocytes induces brain-derived neurotrophic factor expression, which is one of the most important neuroprotective factors.⁵⁸

Accumulating evidence, including the present results, suggests an increasingly important role for microglia and astroglia in the pathogenesis of AD.³⁵ Understanding the physiological functions of these cells is crucial to determining their roles in the disease. There is a further coordinated response between astroglia and microglial cells, but their involvement in proteinopathy spread by the cortical circuitry remains to be elucidated. Microglia activate the proinflammatory cascade and precipitate a failure to degrade the A β protein in AD.⁵⁹ Activated microglia could induce neurotoxic reactive astrocytes, and astrocytes may act to boost molecular peroxidase levels to protect cells from protein misfolding. These changes may also reflect compensatory responses to the neuronal loss observed in AD and indicate a cellular protection mechanism activated in response to this toxic situation.⁶⁰

To our knowledge, this report is the first combining layer-specific stereological studies of neural and glial populations in parallel to proteomic analysis in human EC. Our results indicate general neurodegeneration and microglial cell loss in the whole EC but specific astrogliosis in layers I and II. We detail cell type-specific protein expression patterns in AD. Several novel proteins reported here could play fundamental roles in the pathogenesis of AD and seem to have a functional link with neurons and glial cells, being implicated in synapse function, neuroinflammation, and oxidative stress processes. These results provide new insights into the coordinated control of AD-related proteins and their cell type-specific contributions to disease susceptibility. Future approaches, including an analysis of cases in early stages of the disease, sex-specific differences, and microdissection of specific layers of the EC and the corresponding proteomic analysis, would provide future research challenges.

ACKNOWLEDGMENTS

This study was supported by the UCLM/ERDF (2021-GRIN-31233 to NPND), the Spanish Ministries of Economy and Competitiveness/ERDF (grant no. SAF2016-75768-R), Science and Innovation (grant no. PID2019-108659RB-I00 to AMM), and the Autonomous Government of Castilla-La Mancha/ERDF (grant no. SBPLY/17/180501/000430 to AMM and DSS). SVC and MGR held predoctoral fellowships granted by UCLM/ESF, and VAL held an assistant professorship granted by UCLM/ERDF. The authors are indebted to our donors, and IDIBAPS, BIOBANK-MUR, and BTCIEN integrated in the Spanish National Biobanks Network provided the samples used in this study. This work is part of the doctoral thesis of Veronica Astillero Lopez.

CONFLICTS OF INTEREST

The authors have no conflicts of interest to declare.

ORCID

Isabel Ubeda-Banon  <https://orcid.org/0000-0003-1753-5469>

REFERENCES

- Scheltens P, De Strooper B, Kivipelto M, et al. Alzheimer's disease. *Lancet*. 2021;397:1577-1590.
- Vinters HV. Emerging concepts in Alzheimer's disease. *Annu Rev Pathol*. 2015;10:291-319.
- Hampel H, Hardy J, Blennow K, et al. The Amyloid-beta Pathway in Alzheimer's Disease. *Mol Psychiatry*. 2021.
- Prusiner SB. Cell biology. A unifying role for prions in neurodegenerative diseases. *Science*. 2012;336:1511-1513.
- Peng C, Trojanowski JQ, Lee VM. Protein transmission in neurodegenerative disease. *Nat Rev Neurol*. 2020;16:199-212.
- Braak H, Alafuzoff I, Arzberger T, Kretzschmar H, Del Tredici K. Staging of Alzheimer's disease-associated neurofibrillary pathology using paraffin sections and immunocytochemistry. *Acta Neuropathol*. 2006;112:389-404.
- Gomez-Isla T, Hollister R, West H, et al. Neuronal loss correlates with but exceeds neurofibrillary tangles in Alzheimer's disease. *Ann Neurol*. 1997;41:17-24.
- Pennanen C, Kivipelto M, Tuomainen S, et al. Hippocampus and entorhinal cortex in mild cognitive impairment and early AD. *Neurobiol Aging*. 2004;25:303-310.
- Insausti R, Munoz-Lopez M, Insausti AM, Artacho-Perula E. The human periallocortex: layer pattern in presubiculum, parasubiculum and entorhinal cortex. A review. *Front Neuroanat*. 2017;11:84.
- Insausti R, Tunon T, Sobreviela T, Insausti AM, Gonzalo LM. The human entorhinal cortex: a cytoarchitectonic analysis. *J Comp Neurol*. 1995;355:171-198.
- Witter MP. The perforant path: projections from the entorhinal cortex to the dentate gyrus. *Prog Brain Res*. 2007;163:43-61.
- Ubeda-Banon I, Saiz-Sanchez D, Flores-Cuadrado A, et al. The human olfactory system in two proteinopathies: Alzheimer's and Parkinson's diseases. *Transl Neurodegener*. 2020;9:22.
- Squire LR, Stark CE, Clark RE. The medial temporal lobe. *Annu Rev Neurosci*. 2004;27:279-306.
- Pini L, Pievani M, Bocchetta M, et al. Brain atrophy in Alzheimer's disease and aging. *Ageing Res Rev*. 2016;30:25-48.
- West MJ, Gundersen HJ. Unbiased stereological estimation of the number of neurons in the human hippocampus. *J Comp Neurol*. 1990;296:1-22.
- West MJ, Coleman PD, Flood DG, Troncoso JC. Differences in the pattern of hippocampal neuronal loss in normal ageing and Alzheimer's disease. *Lancet*. 1994;344:769-772.
- von Gunten A, Kövari E, Bussièrè T, et al. Cognitive impact of neuronal pathology in the entorhinal cortex and CA1 field in Alzheimer's disease. *Neurobiol Aging*. 2006;27, 270-277.
- Gomez-Isla T, Price JL, McKeel DW Jr, Morris JC, Growdon JH, Hyman BT. Profound loss of layer II entorhinal cortex neurons occurs in very mild Alzheimer's disease. *J Neurosci*. 1996;16:4491-4500.
- Price JL, Ko AI, Wade MJ, Tsou SK, McKeel DW, Morris JC. Neuron number in the entorhinal cortex and CA1 in preclinical Alzheimer disease. *Arch Neurol*. 2001;58:1395-1402.
- Kordower JH, Chu Y, Stebbins GT, et al. Loss and atrophy of layer II entorhinal cortex neurons in elderly people with mild cognitive impairment. *Ann Neurol*. 2001;49:202-213.
- Dominguez-Alvaro M, Montero-Crespo M, Blazquez-Llorca L, DeFelipe J, Alonso-Nanclares L. 3D ultrastructural study of synapses in the human entorhinal cortex. *Cereb Cortex*. 2021;31:410-425.
- Witter MP, Moser EI. Spatial representation and the architecture of the entorhinal cortex. *Trends Neurosci*. 2006;29:671-678.
- Braak H, Del Tredici K. The preclinical phase of the pathological process underlying sporadic Alzheimer's disease. *Brain*. 2015;138:2814-2833.
- Mallio CA, Schmidt R, de Reus MA, et al. Epicentral disruption of structural connectivity in Alzheimer's disease. *CNS Neurosci Ther*. 2015;21:837-845.
- Taipà R, Ferreira V, Brochado P, et al. Inflammatory pathology markers (activated microglia and reactive astrocytes) in early and late onset

- Alzheimer's disease: a post mortem study. *Neuropathol Appl Neurobiol.* 2018;44:298-313.
26. Kobayashi E, Nakano M, Kubota K, et al. Activated forms of astrocytes with higher GLT-1 expression are associated with cognitive normal subjects with Alzheimer's pathology in human brain. *Sci Rep.* 2018;8:1712.
 27. Xu J, Patassini S, Rustogi N, et al. Regional protein expression in human Alzheimer's brain correlates with disease severity. *Commun Biol.* 2019;2:43.
 28. Mendonca CF, Kuras M, Nogueira FCS, et al. Proteomic signatures of brain regions affected by tau pathology in early and late stages of Alzheimer's disease. *Neurobiol Dis.* 2019;130:104509.
 29. Jia Y, Wang X, Chen Y, Qiu W, Ge W, Ma C. Proteomic and transcriptomic analyses reveal pathological changes in the entorhinal cortex region that correlate well with dysregulation of ion transport in patients with Alzheimer's disease. *Mol Neurobiol.* 2021;58:4007-4027.
 30. Ferrer I, Andrés-Benito P, Ausín K, et al. Dysregulated protein phosphorylation: a determining condition in the continuum of brain aging and Alzheimer's disease. *Brain Pathol.* 2021;31, e12996.
 31. Villar-Conde S, Astillero-Lopez V, Gonzalez-Rodriguez M, et al. The human hippocampus in Parkinson's disease: an integrative stereological and proteomic study. *J Parkinsons Dis.* 2021.
 32. Mai JK, Paxinos G & Voss, T. *Atlas of the Human Brain.* 3rd ed. Elsevier; 2008.
 33. Spina S, La Joie R, Petersen C, et al. Comorbid neuropathological diagnoses in early versus late-onset Alzheimer's disease. *Brain.* 2021;144:2186-2198.
 34. Dumoulin SO. Layers of neuroscience. *Neuron.* 2017;96:1205-1206.
 35. Henstridge CM, Hyman BT, Spires-Jones TL. Beyond the neuron-cellular interactions early in Alzheimer's disease pathogenesis. *Nat Rev Neurosci.* 2019;20:94-108.
 36. Qasim SE, Miller J, Inman CS, et al. Memory retrieval modulates spatial tuning of single neurons in the human entorhinal cortex. *Nat Neurosci.* 2019;22:2078-2086.
 37. Nilssen ES, Doan TP, Nigro MJ, Ohara S, Witter MP. Neurons and networks in the entorhinal cortex: a reappraisal of the lateral and medial entorhinal subdivisions mediating parallel cortical pathways. *Hippocampus.* 2019;29:1238-1254.
 38. Kibro-Flatmoen A, Lagartos-Donate MJ, Aman Y, Edison P, Witter MP, Fang EF. Re-emphasizing early Alzheimer's disease pathology starting in select entorhinal neurons, with a special focus on mitophagy. *Ageing Res Rev.* 2021;67:101307.
 39. Yamashita N, Ilg EC, Schafer BW, Heizmann CW, Kosaka T. Distribution of a specific calcium-binding protein of the S100 protein family, S100A6 (calcyclin), in subpopulations of neurons and glial cells of the adult rat nervous system. *J Comp Neurol.* 1999;404:235-257.
 40. Tian ZY, Wang CY, Wang T, Li YC, Wang ZY. Glial S100A6 degrades beta-amyloid aggregation through targeting competition with zinc ions. *Ageing Dis.* 2019;10:756-769.
 41. Cristovao JS, Gomes CM. S100 proteins in Alzheimer's disease. *Front Neurosci.* 2019;13:463.
 42. Cho K, Cho MH, Seo JH, et al. Calpain-mediated cleavage of DARPP-32 in Alzheimer's disease. *Ageing Cell.* 2015;14:878-886.
 43. Ji C, Tang M, Zeidler C, Hohfeld J, Johnson GV. BAG3 and SYNPO (synaptopodin) facilitate phospho-MAPT/Tau degradation via autophagy in neuronal processes. *Autophagy.* 2019;15:1199-1213.
 44. Power JH, Asad S, Chataway TK, et al. Peroxiredoxin 6 in human brain: molecular forms, cellular distribution and association with Alzheimer's disease pathology. *Acta Neuropathol.* 2008;115:611-622.
 45. Pankiewicz JE, Diaz JR, Marta-Ariza M, Lizinczyk AM, Franco LA, Sadowski MJ. Peroxiredoxin 6 mediates protective function of astrocytes in Abeta proteostasis. *Mol Neurodegener.* 2020;15:50.
 46. Wang X, Wang W, Li L, Perry G, Lee HG, Zhu X. Oxidative stress and mitochondrial dysfunction in Alzheimer's disease. *Biochim Biophys Acta.* 2014;1842:1240-1247.
 47. Sayas CL, Avila J. GSK-3 and tau: a key duet in Alzheimer's Disease. *Cells.* 2021;10, 721.
 48. Kettunen P, Larsson S, Holmgren S, et al. Genetic variants of GSK3B are associated with biomarkers for Alzheimer's disease and cognitive function. *J Alzheimers Dis.* 2015;44:1313-1322.
 49. Prati F, De Simone A, Bisignano P, et al. Multitarget drug discovery for Alzheimer's disease: triazinones as BACE-1 and GSK-3 β inhibitors. *Angew Chem Int Ed Engl.* 2015;54:1578-1582.
 50. Margiotta A. Role of SNAREs in neurodegenerative diseases. *Cells.* 2021:10.
 51. Tsuji S, Hase T, Yachie-Kinoshita A, et al. Artificial intelligence-based computational framework for drug-target prioritization and inference of novel repositionable drugs for Alzheimer's disease. *Alzheimers Res Ther.* 2021;13:92.
 52. Huang M, Darvas M, Keene CD, Wang Y. Targeted quantitative proteomic approach for high-throughput quantitative profiling of small GTPases in brain tissues of Alzheimer's disease patients. *Anal Chem.* 2019;91:12307-12314.
 53. Calderon-Garcidueñas AL, Duyckaerts C. Alzheimer disease, , eds. *Handb of Clin Neurol.* 145 ; 2017:325-337.
 54. Qin S, Hu XY, Xu H, Zhou JN. Regional alteration of synapsin I in the hippocampal formation of Alzheimer's disease patients. *Acta Neuropathol.* 2004;107:209-215.
 55. Proctor DT, Coulson EJ, Dodd PR. Reduction in post-synaptic scaffolding PSD-95 and SAP-102 protein levels in the Alzheimer's inferior temporal cortex is correlated with disease pathology. *J Alzheimers Dis.* 2010;21:795-811.
 56. Perea G, Navarrete M, Araque A. Tripartite synapses: astrocytes process and control synaptic information. *Trends Neurosci.* 2009;32:421-431.
 57. Sloan SA, Darmanis S, Huber N, et al. Human astrocyte maturation captured in 3D cerebral cortical spheroids derived from pluripotent stem cells. *Neuron.* 2017;95:779-790.e6.
 58. Hong Y, Zhao T, Li XJ, Li S. Mutant huntingtin impairs BDNF release from astrocytes by disrupting conversion of Rab3a-GTP into Rab3a-GDP. *J Neurosci.* 2016;36:8790-8801.
 59. Salter MW, Stevens B. Microglia emerge as central players in brain disease. *Nat Med.* 2017;23:1018-1027.
 60. Sfera A, Gradini R, Cummings M, Diaz E, Price AI, Osorio C. Rusty microglia: trainers of innate immunity in Alzheimer's disease. *Front Neurol.* 2018;9:1062.

SUPPORTING INFORMATION

Additional supporting information may be found in the online version of the article at the publisher's website.

How to cite this article: Astillero-Lopez V, Gonzalez-Rodriguez M, Villar-Conde S, et al. Neurodegeneration and astrogliosis in the entorhinal cortex in Alzheimer's disease: Stereological layer-specific assessment and proteomic analysis. *Alzheimer's Dement.* 2021;1-13. <https://doi.org/10.1002/alz.12580>